Nanoscale

ROYAL SOCIETY OF CHEMISTRY

PAPER

View Article Online
View Journal | View Issue

Cite this: *Nanoscale*, 2024, **16**, 18375

An integrated dual-gradient host facilitates oriented bottom-up lithium growth in lithium metal anodes†

Zhuzhu Du,[a,b] Xin Chen,[b] Ying Zhao,[c] Yuhang Liu*[b] and Wei Ai *[b]

Integrated gradient hosts, composed of poorly conductive frameworks on copper current collectors, have been extensively explored for the development of Li metal anodes (LMAs). Despite their potential, high Li nucleation overpotentials and slow interface kinetics often lead to inferior performance. Herein, we combine electrospinning and electrodeposition to create an integrated gradient host, namely OPAN/rGO-Cu_2O/Cu. This involves electrodeposition of graphene oxide onto copper foil, reacting *in situ* to form a lithiophilic rGO-Cu_2O layer, which is then covered with an oxidized polyacrylonitrile (OPAN) nanofiber layer, establishing conductivity and lithiophilicity dual gradients. The insulating OPAN top layer blocks electron transmission to the surface and prevents Li deposition, while the lithiophilic rGO-Cu_2O layer facilitates Li ion transport to the bottom and reduces the nucleation barrier, both of which promote uniform Li deposition from bottom to top. As a result, the battery achieves an average coulombic efficiency of 98.4% over 500 cycles at 1 mA cm^{-2}, and the symmetric cell sustains an ultra-long cycle life of 1600 h with a minimal polarization voltage of 12 mV. When paired with a $LiFePO_4$ cathode, the full cell demonstrates a capacity retention of 92.6% after 300 cycles at 1 C, with an average capacity decay rate of just 0.025% per cycle. This innovative approach offers a promising pathway for developing high-performance LMAs.

Received 17th July 2024,
Accepted 26th August 2024

DOI: 10.1039/d4nr02963a

rsc.li/nanoscale

[a]*School of Materials Science and Engineering & Institute of Flexible Electronics and Intelligent Textile, Xi'an Polytechnic University, Xi'an 710048, China*
[b]*Frontiers Science Center for Flexible Electronics & Shaanxi Institute of Flexible Electronics, Northwestern Polytechnical University, Xi'an 710072, China. E-mail: iamwai@nwpu.edu.cn, liuyh@mail.nwpu.edu.cn*
[c]*Xi'an Hongxing Electronic Paste Technology Co., Ltd, Xi'an 710199, China*
†Electronic supplementary information (ESI) available. See DOI: https://doi.org/10.1039/d4nr02963a

Wei Ai

Wei Ai received his Ph.D. and M.S. degrees from Nanyang Technological University and Nanjing University of Posts and Telecommunications, respectively. After working as a research associate at Nanyang Technological University, he joined the Institute of Flexible Electronics at Northwestern Polytechnical University. His research interests focus on electrochemical materials and technologies, new energy devices, flexible intelligence technologies, etc.

1. Introduction

Li metal anodes (LMAs) are considered one of the most promising options for next-generation high-energy-density batteries due to their high theoretical capacity and low electrode potential.[1,2] However, the practical implementation of LMAs has yet to be developed because of the low coulombic efficiency (CE) and safety hazards arising from the unrestricted dendrite growth, cracking/rebuilding of the solid electrolyte interphase (SEI) and infinite volume fluctuations during cycling.[3,4] To address these issues, host materials with high specific surface areas and rich porosity have been developed, which can help distribute the Li ions more evenly during deposition and reduce the chances of dendrite formation.[5–7] Moreover, the large surface area and porosity of hosts can accommodate the volume expansion of LMAs, improving the structural stability of the electrode.[8–10] Despite these advances, LMAs still face numerous challenges that need to be overcome before they can be safely and efficiently used.

The study of LMA hosts has centred around introducing lithiophilic sites or designing pore structures. Generally, introducing lithiophilic components like Au,[11] Ag,[12] ZnO,[13] Cu_2O,[14] Cu_3P,[15] *etc.* into the hosts can reduce the polarization related to Li nucleation and deposition because of their high affinity

for Li, which can promote homogeneous Li nucleation and growth and thereby help prevent dendrite formation. Engineering pore structures by tuning the size, depth and pore tortuosity can optimize the transport pathways of Li ions and mitigate the volume fluctuations during Li plating/stripping.[16,17] Considering the short diffusion distance and higher Li ion concentration at the electrode–separator interface, Li metal prefers to deposit on the top of the hosts, particularly at high current densities, which can initiate the formation of Li dendrites.[18,19] One proposed solution is to give the hosts gradient properties, which would guide Li to deposit at the bottom instead of the surface. However, for integrated gradient hosts composed of poorly conductive frameworks covered on a copper (Cu) current collector, high Li nucleation overpotentials are noted.[20,21] Meanwhile, the weak interaction between the poorly conductive framework and Cu foil results in slow interface kinetics, further complicating the process of Li deposition.[22,23] Therefore, more research and innovation are needed to overcome the remaining challenges associated with the gradient hosts of LMAs.

In this work, we construct a composited conductivity/lithiophilicity dual-gradient host by covering Cu foil with electrodeposited reduced graphene oxide (rGO), followed by an oxidized polyacrylonitrile (OPAN) nanofiber layer. On one hand, the Cu foil, *in situ* generated rGO-Cu_2O, and OPAN nanofiber layers form a conductivity gradient, with conductivity attenuating upwards. This gradient controls the distribution of electrons. On the other hand, the rGO-Cu_2O layer and OPAN nanofiber layer together form a lithiophilicity gradient, which regulates the distribution of Li ions. By controlling the distribution of both electrons and Li ions, this dual-gradient structure promotes a bottom-up Li deposition manner, reducing the risk of dendrite formation. Moreover, the electrostatic interaction between the rGO-Cu_2O layer and the OPAN nanofiber layer enhances the interface dynamics, resulting in better Li deposition. As a result, the OPAN/rGO-Cu_2O/Cu (termed OGCC) host can work for 500 cycles with an average CE of 98.4% at a current density of 1.0 mA cm^{-2} and a capacity of 1 mA h cm^{-2}. Even at 3.0 mA cm^{-2} for 3 mA h cm^{-2}, OGCC can still afford a high CE of 98.2% after 110 cycles. When the OGCC@Li anode is paired with a $LiFePO_4$ (LFP) cathode, the resulting full cell demonstrates exceptional cycling stability, with over 90% capacity retention after 300 cycles at 1.0 C (1 C = 170 mA g^{-1}). This work indicates that dual-gradient hosts offer a promising approach for overcoming the challenges of LMAs towards high-energy-density batteries.

2. Experimental

2.1. Preparation of OGCC

Initially, 50 mg of graphene oxide (GO) was dispersed in 50 mL of deionized water and subjected to sonication for 1.5 h. A Cu foil measuring 3 cm × 4 cm was then immersed in the GO suspension, and GO was deposited onto its surface using chronoamperometry at 3 V for 40 s to fabricate the rGO-Cu_2O layer. Next, 0.5244 g of polyacrylonitrile (PAN) with a molecular weight of 150 000 was dissolved in 5 mL of dimethylformamide and stirred at 30 °C for 24 h. This solution was then electrospun at 13.5 kV, with a distance of 10 cm and a flow rate of 1 mL h^{-1} to form a PAN film. After electrospinning, the PAN film was carefully removed from the substrate and subjected to an oxidation process in air at 240 °C for 2 h, with a temperature increase of 2 °C per minute, to convert it into OPAN. Finally, the OPAN film was directly layered onto rGO-Cu_2O/Cu to assemble OGCC.

2.2 Characterization studies

X-ray powder diffraction (XRD) patterns were collected using a Shimadzu XRD-7000s diffractometer equipped with Cu Kα radiation (λ = 0.154056 nm). Scanning electron microscopy (SEM) images were captured on an FEI Verios G4 microscope at an accelerating voltage of 5 kV. Contact angles for the electrolytes were measured with a DSA25 contact angle tester.

2.3. Electrochemical characterization studies

All coin cells were assembled using standard CR2032 coin-type cells in a glovebox filled with highly purified argon (H_2O < 0.1 ppm and O_2 < 0.1 ppm). The electrodes were cut into circular pieces with a diameter of 12 mm. A Celgard-2500 polypropylene film served as the separator. The electrolyte comprised 1 M lithium bis(trifluoromethanesulfonyl) imide in a dioxolane/dimethoxyethane mixture (1 : 1 by volume) with 2 wt% $LiNO_3$. To assess the CE and Li plating/stripping behavior, OGCC||Li half cells were assembled. For the cyclability tests, 10 mA h cm^{-2} of Li was initially deposited onto the OGCC host at a current density of 0.5 mA cm^{-2}, before assembling the OGCC@Li||OGCC@Li cells. Additionally, Cu foil||Li half cells and Li||Li symmetric cells were fabricated for comparison. To explore the practical application of the OGCC@Li electrode, a LFP||OGCC-Li full cell was assembled. The LFP working electrodes were prepared by mixing LFP, polyvinylidene difluoride, and super P in an 8 : 1 : 1 ratio in *N*-methyl-2-pyrrolidone and then coating the slurry onto an Al foil, maintaining a mass loading of ~3 mg cm^{-2}. All cells underwent preconditioning at 0.2 mA cm^{-2} for five cycles between 0 and 1 V to eliminate surface contaminants on the working electrodes. All electrochemical tests were conducted using a NEWARE battery testing system and a CHI 760E electrochemical workstation.

3. Results and discussion

Fig. 1a presents schematic illustrations for the fabrication of the OGCC host. Initially, rGO-Cu_2O/Cu was prepared by electrodeposition of GO onto a Cu foil. This setup uses a stainless-steel mesh as the counter electrode, a saturated calomel electrode as the reference electrode, a Cu foil as the working electrode, and a GO suspension as the electrolyte.[24,25] During this process, GO reacts *in situ* with the Cu foil to form lithiophilic Cu_2O and rGO on the surface. The resultant rGO-Cu_2O/Cu elec-

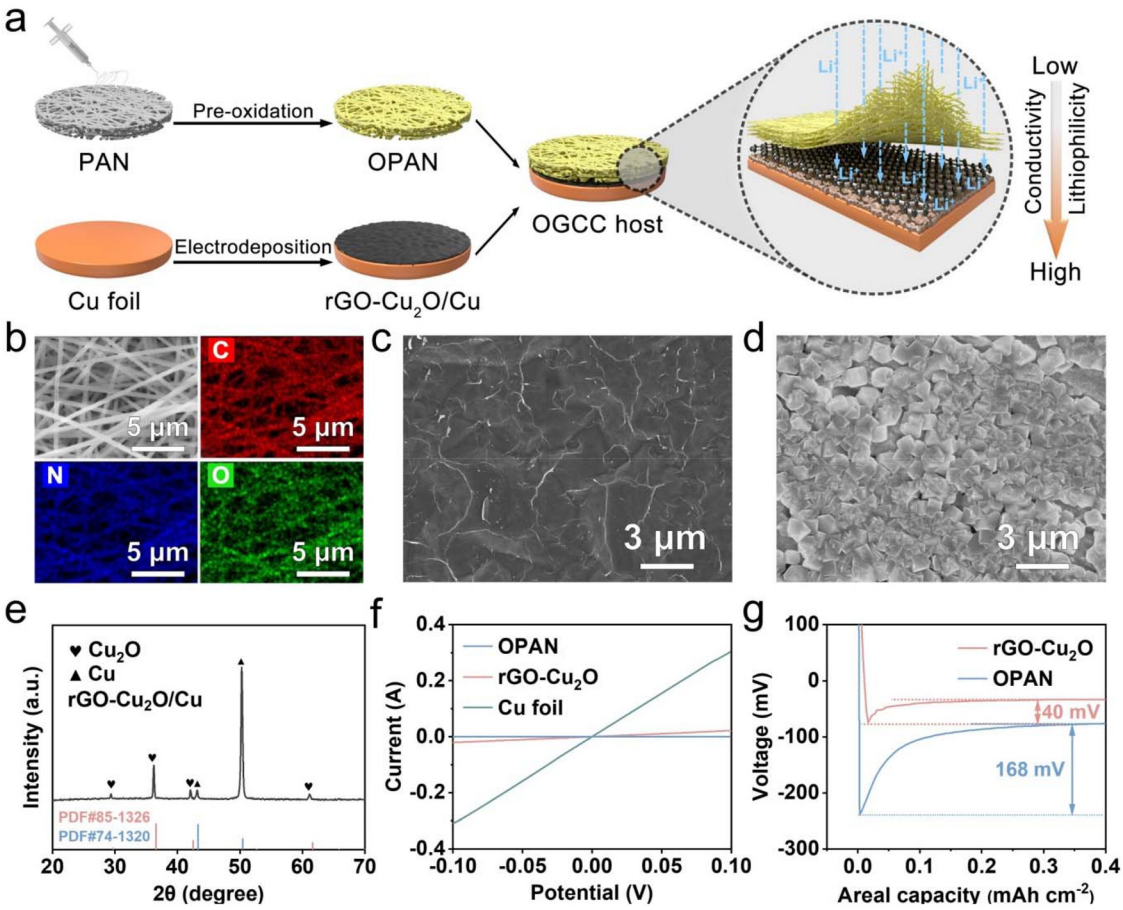

Fig. 1 (a) Schematic illustration of the OGCC host. SEM image of (b) OPAN nanofibers, (c) rGO, and (d) Cu_2O. (e) XRD pattern of Cu_2O. (f) Voltage–capacity curves of OPAN, rGO-Cu_2O, and Cu foil. (g) Nucleation overpotentials of Li deposition at 1 mA cm^{-2}.

trode was then dried in a vacuum oven. Subsequently, a high-strength OPAN film, produced by air oxidation of the electrospun PAN nanofiber film, was placed directly on rGO-Cu_2O/Cu and shaped into circular electrodes with a diameter of 12 mm. This assembly features a top-down increasing conductivity gradient, with the insulating OPAN layer, the moderately conductive rGO-Cu_2O layer, and the highly conductive Cu foil. Additionally, the OPAN and rGO-Cu_2O layers contribute to a top-down increasing lithiophilic gradient. Accordingly, a dual gradient structure for both conductivity and lithiophilicity is established.

Fig. S1a and S1b† show the photographs of the PAN film before and after oxidation, respectively. Initially, the colour of the PAN film is white, which changes to brown upon oxidation. SEM images reveal that the nanofiber structure in the films remains consistent before and after oxidation (Fig. S1c and S1d†).[13,26] Energy-dispersive X-ray spectroscopy (EDS) analyses indicate an even distribution of carbon (C), nitrogen (N), and oxygen (O) elements within the OPAN film, suggesting that oxidation incorporates oxygen-containing functional groups, such as C═O, O–H, *etc*. (Fig. 1b). This structural modification helps distribute Li ion flux evenly, prevents local ion aggregation, and consequently inhibits the formation of Li dendrites. Further studies involve SEM characterization of the Cu foil surface before and after GO electrodeposition. In contrast to the smooth surface of the pristine Cu foil, the electrodeposited surface exhibits a dense layer of graphene sheets (Fig. 1c and S2†). Upon removing this graphene layer, numerous cubic particles become visible on the Cu surface (Fig. 1d). XRD testing reveals, in addition to the characteristic peaks of Cu, peaks corresponding to the (110), (111), (200), and (220) crystal planes of Cu_2O at 29.7, 36.6, 42.5, and 61.6°, respectively (Fig. 1e), indicative of the reaction between GO and Cu that forms rGO and Cu_2O.[27] Contact angle measurements demonstrate a significant improvement in electrolyte uptake on the rGO-Cu_2O coated Cu foil, exhibiting a contact angle of 0° that is a marked decrease from the 30° observed with the pristine Cu foil (Fig. S3†). This uniform structure promotes even Li ion flux, ensuring consistent Li deposition.

To investigate the presence of conductivity and lithiophilicity gradients, we initially assessed the conductivity of OPAN, rGO-Cu_2O, and Cu foil. The voltage–capacity curves demonstrate a sequential increase in conductivity from OPAN through rGO-Cu_2O to Cu foil, indicating an upward gradient of conductivity within the OGCC host (Fig. 1f). Concurrently, at a current density of 1 mA cm^{-2}, the Li nucleation overpotential

for rGO-Cu_2O is markedly low at 40 mV, substantially less than that of OPAN (168 mV, Fig. 1g). This suggests increased lithiophilicity from top to bottom in the OGCC host. Therefore, both electronic conductivity and Li nucleation capability enhance progressively from the top towards the bottom, achieving a dual gradient of conductivity and lithiophilicity.[28] This gradient effectively concentrates Li ions and electrons at the bottom, facilitating stable bottom-up Li deposition (refer to subsequent discussion).

To explore Li deposition behavior, varying amounts of Li metal were electrodeposited into the OGCC host at a current density of 0.5 mA cm^{-2}. Post-deposition, the battery was disassembled, and the morphology of the Li deposits was examined using *ex situ* SEM. When 3 mA h cm^{-2} of Li was deposited, the top-view SEM image reveals that the OPAN nanofibers on the upper layer retain their original structure, with no visible Li metal on the electrode surface (Fig. S4a†). The side-view SEM image shows Li concentrated at the bottom of OGCC (Fig. 2a). Increasing the deposition capacity to 5 mA h cm^{-2} results in an even upward progression of Li within OGCC, maintaining a dendrite-free surface (Fig. 2b and S4b†). Even at 10 mA h cm^{-2}, Li continues to deposit smoothly and uniformly upward (Fig. 2c and S4c†). In contrast, at a deposition capacity of 3 mA h cm^{-2} on the Cu foil, large Li dendrites are clearly visible in both top and side views (Fig. 2d and S5a†). As the capacity increases to 5 mA h cm^{-2}, rapid dendrite growth and significant electrode thickening occur, accompanied by electrode cracking (Fig. 2e and S5b†). At 10 mA h cm^{-2}, the Cu foil is overwhelmed with Li dendrites about 2 μm in diameter, which intertwine to form a loose, porous structure that leads to severe electrode cracking (Fig. 2f and S5c†). These observations confirm that increasing deposition capacity inside OGCC results in a bottom-up deposition pattern, effectively suppressing Li dendrite formation thanks to the conductivity/lithiophilicity dual-gradient structure (Fig. 2g). Conversely, uneven current distribution on the Cu foil surface causes Li ions to accumulate and preferentially reduce at high current density locations, leading to dendrite formation (Fig. 2h). Furthermore, the tip effect intensifies this issue, as the dendrite tips become new local hotspots, exacerbating uneven Li deposition and promoting further dendrite growth.[3]

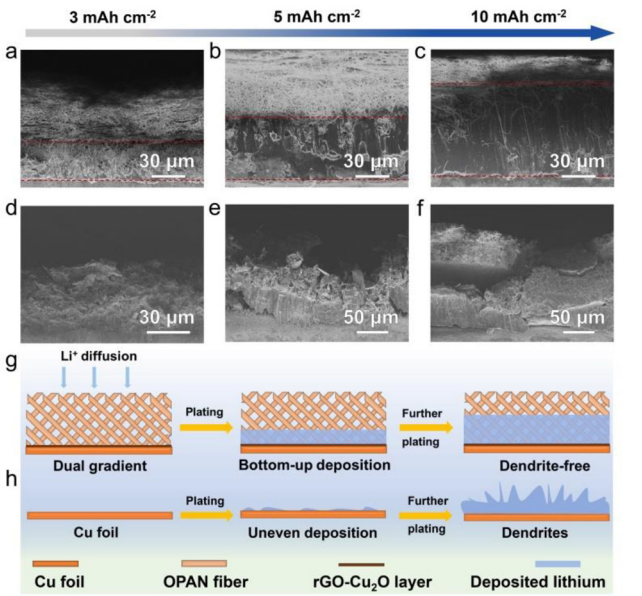

Fig. 2 Side-view SEM images of Li deposition in (a–c) OGCC and (d–f) bare Cu foil at 0.5 mA cm^{-2}: (a and d) 3 mA h cm^{-2}; (b and e) 5 mA h cm^{-2}; and (c and f) 10 mA h cm^{-2}. Schematic illustrations of Li deposition in (g) OGCC and (h) bare Cu foil.

To observe the Li plating process in real time, *in situ* optical microscopy observations were performed. Metallic Li was deposited on both OGCC and Cu foil for 60 min at a current density of 1 mA cm^{-2}. In the OGCC host, Li deposition is clearly visible, accumulating uniformly and flatly at the bottom after just 10 min (Fig. 3a). As the deposition continues, the Li maintains its smooth morphology throughout OGCC, demonstrating a bottom-up, dendrite-free deposition pattern that begins from the bottom of the host and gradually extends upward. In stark contrast, visible Li dendrites begin forming on the Cu foil within the first 10 min of deposition (Fig. 3b). With increasing deposition time, the dendrite growth on the Cu foil intensifies, eventually leading to complete coverage of the surface with dendrites. These findings align with those observed in *ex situ* SEM analyses, highlighting the stark differences in deposition behavior between the two materials.

The CE and cycling performance of the host were evaluated using half-cells assembled with either OGCC or Cu foil as the working electrode. As depicted in Fig. 4a, under conditions of 1 mA cm^{-2} for 1 mA h cm^{-2}, the OGCC host consistently delivers stable cycling for 500 cycles, maintaining an average CE of 98.4%. In contrast, the CE of Cu foil rapidly declines after just 100 cycles. Under increased conditions of 3 mA cm^{-2} for 3 mA h cm^{-2}, the OGCC host still manages stable cycling for 110 cycles, achieving an average CE of 98.2% (Fig. 4b). However, the Cu foil exhibits significant fluctuations in CE at the start, rapidly deteriorating after 50 cycles. This performance disparity is attributed to the dual-gradient structure of OGCC, which regulates Li deposition behavior, unlike Cu foil, where Li dendrite growth and the formation of inactive Li lead to rapid CE degradation.[29,30] Fig. S6a† illustrates the nucleation overpotentials for OGCC and Cu foil at 1 mA cm^{-2}, where OGCC exhibits a significantly lower overpotential of 68 mV compared to 171 mV for Cu foil. Additionally, under the same testing conditions, the capacity–voltage curves for the OGCC electrode exhibit high consistency across various cycles, unlike the poor overlap observed with Cu foil (Fig. S6b and S6c†). This is largely due to the lithiophilic rGO-Cu_2O layer within OGCC, which effectively lowers the Li nucleation barrier. Moreover, the dual-gradient design of OGCC enables uniform Li deposition, minimizes polarization during deposition, and substantially reduces the risks of Li dendrite and inactive Li formation, resulting in superior cycle reversibility.

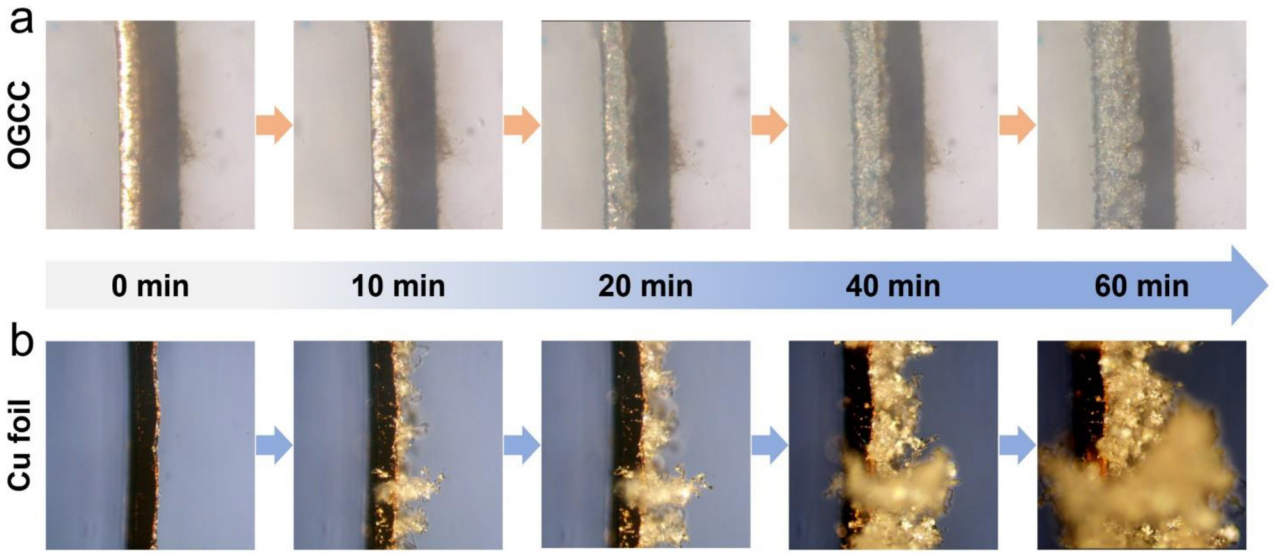

Fig. 3 *In situ* optical images of the Li plating process in (a) OGCC and (b) bare Cu foil.

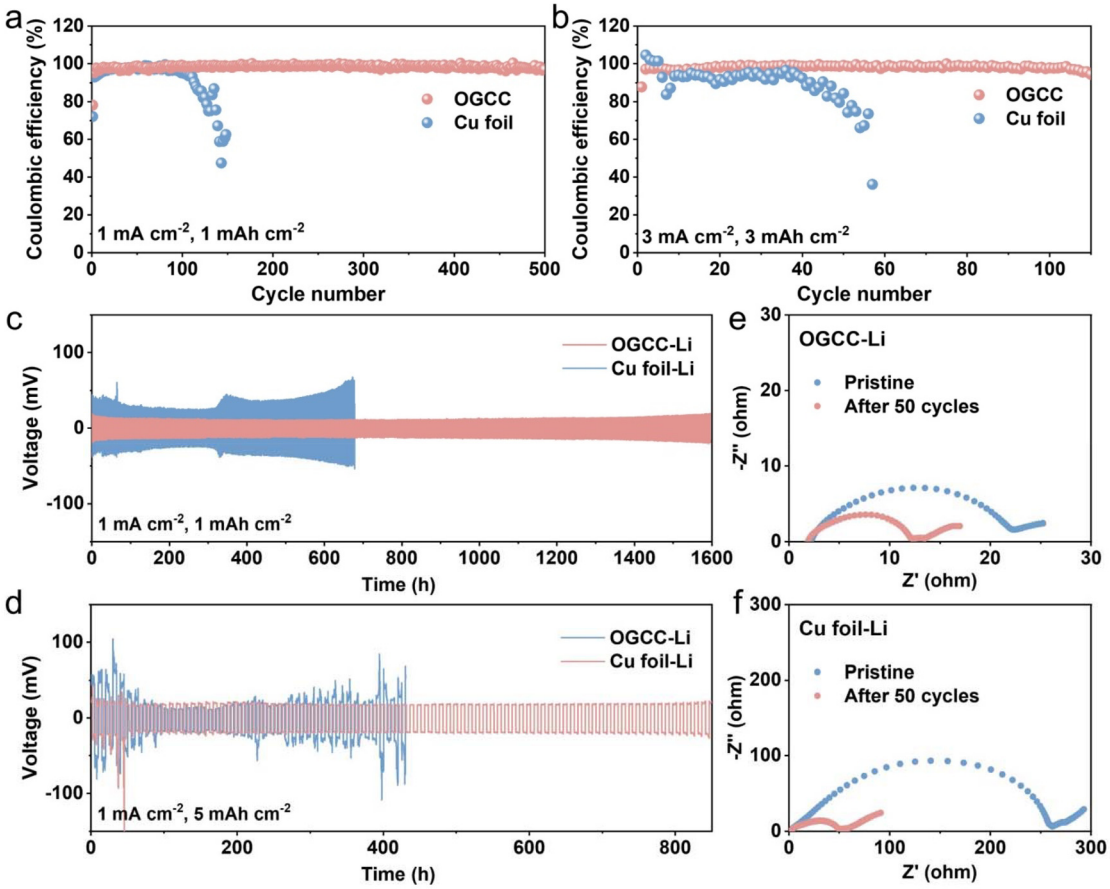

Fig. 4 (a) CE of half cells based on OGCC and Cu foil (a) at 1 mA cm^{-2} for 1 mA h cm^{-2} and (b) at 3 mA cm^{-2} for 3 mA h cm^{-2}. Long-term cycling performance of symmetric cells based on OGCC-Li and Cu foil-Li (c) at 1 mA cm^{-2} for 1 mA h cm^{-2} and (d) at 1 mA cm^{-2} for 5 mA h cm^{-2}. A Nyquist plot of the impedance of symmetric cells based on (e) OGCC-Li and (f) Cu foil-Li before cycling and after 50 cycles at 1 mA cm^{-2}.

To assess the impact of OGCC and Cu foil on the cycling performance of LMAs, their surface morphologies were analysed after various cycles. Under conditions of 1 mA cm^{-2} for 1 mA h cm^{-2}, Fig. S7a† reveals that no Li metal is present on the surface of OGCC after one cycle, a finding corroborated by its accompanying photograph, which confirms the absence of Li deposition on the electrode surface. After 50 cycles, the OGCC surface remains intact with no Li deposition observed, and the electrode surface shows little change (Fig. S7b†). In contrast, Li dendrites are evident on the surface of the Cu foil after just one cycle, with photographs showing uneven Li deposition (Fig. S7c†). This unevenness is attributed to the irregular distribution of electrons and Li ions on the Cu foil, leading to uneven Li nucleation.[31] Li ions continue to preferentially reduce at these nucleation sites, forming dendrites. After 50 cycles, the surface of the Cu foil turns black, displaying a significant accumulation of loose Li dendrites and inactive Li, along with noticeable electrode powdering (Fig. S7d†). Such changes result in significant battery polarization and a reduction in CE. These findings demonstrate that OGCC effectively regulates Li deposition, directing the preferential reduction of Li metal at the bottom of the host material. This regulation prevents the formation of Li dendrites and inactive Li on the electrode surface, thereby enhancing the cycling stability of the LMA.[32]

Symmetric cells were utilized to assess the cycling stability of OGCC-Li and Cu foil-Li electrodes, which were prepared by depositing 7 mA h cm^{-2} of Li onto each substrate at a current density of 0.5 mA cm^{-2}. As depicted in Fig. 4c, under conditions of 1 mA cm^{-2} for 1 mA h cm^{-2}, the polarization voltage of OGCC-Li is approximately 12 mV, and it maintains stable cycling for 1600 h. In contrast, Cu foil-Li starts with an initial polarization voltage of about 29 mV, which escalates to 40 mV after 300 h, and then spikes sharply after 670 h due to extensive formation of inactive Li, SEI rupture, and electrolyte consumption, leading to battery failure. Furthermore, local curves in Fig. S8a† reveal that the Cu foil-Li electrode exhibits peak-like voltage curves, which may be ascribed to the dissolution of Li dendrites and the formation of dead Li. Meanwhile, the OGCC-Li electrode consistently sustains the flat voltage curves with a low overpotential of 14 mV, suggesting a good regulatory effect for Li deposition (Fig. S8b†). When the deposition

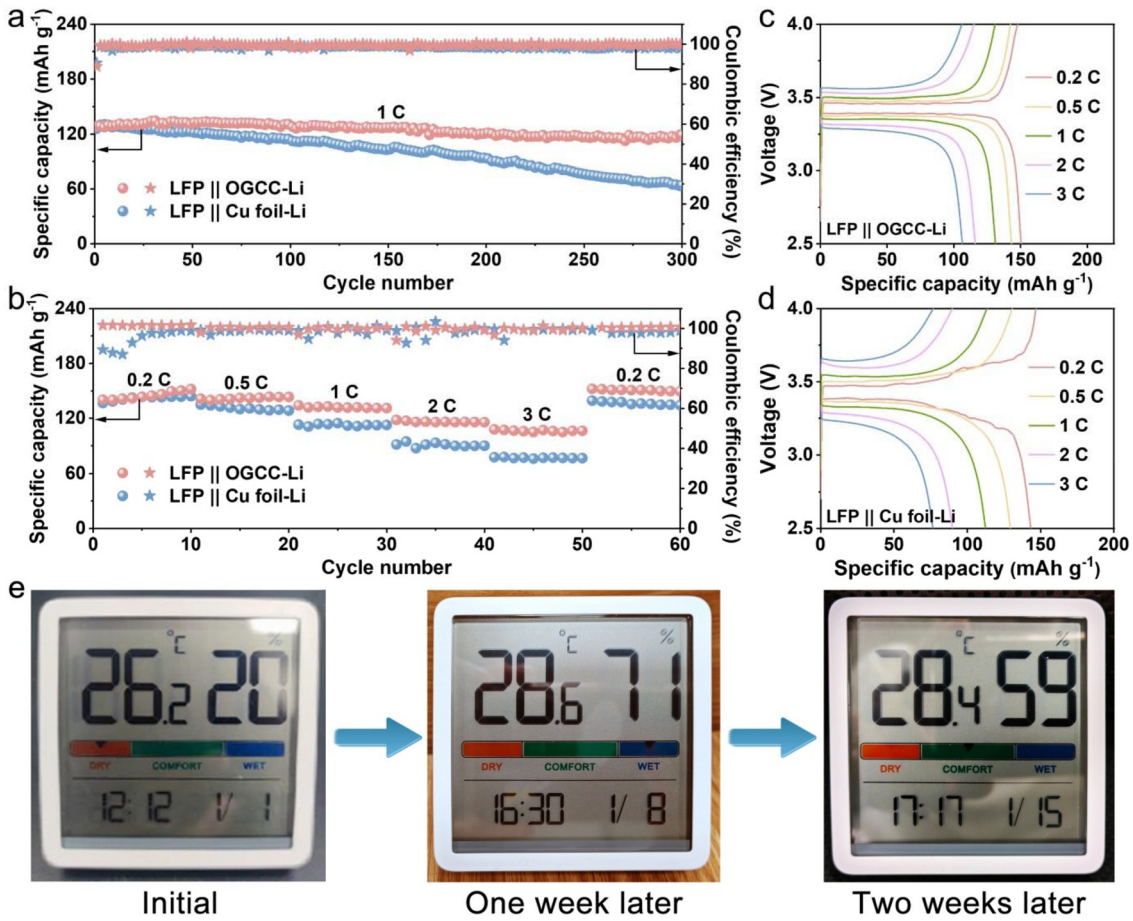

Fig. 5 (a) Long-term cycling and (b) rate performance of LFP||OGCC-Li in comparison with the LFP||Cu foil-Li full cells. The charge–discharge curves of (c) LFP||OGCC-Li and (d) LFP||Cu foil-Li full cells at different rates. (e) Digital photographs of the LFP||OGCC-Li full cell for powering a hygrothermograph for two weeks.

capacity is increased to 5 mA h cm^{-2}, the OGCC-Li anode still exhibits a low polarization voltage of ~14 mV and cycles stably for over 800 h (Fig. 4d). In contrast, the Cu foil-Li anode shows poor cycling stability with significant fluctuations in polarization voltage, underscoring the superior performance of the OGCC-Li anode. Electrochemical impedance spectroscopy (EIS) was conducted on the symmetric cells to evaluate the electrode–electrolyte interfacial resistance. It can be seen that the interfacial impedance of the OGCC-Li electrode before and after cycling changes from 21 to 10 Ω, respectively (Fig. 4e). In comparison, the Cu foil-Li electrode exhibits much higher interfacial impedances of about 260 Ω before cycling and 48 Ω after 50 cycles (Fig. 4f). This disparity is attributed to the conductivity/lithiophilicity dual-gradient structure of OGCC, which prevents Li dendrite formation, mitigates volume expansion, stabilizes the SEI, and facilitates rapid interfacial ion transfer. In line with EIS findings, the SEM images of the cycled electrodes reveal that the surface of the OGCC-Li electrode remains smooth and flat without Li dendrites, whereas the Cu foil-Li electrode is covered with numerous Li dendrites and inactive Li (Fig. S9†). These observations corroborate the EIS analysis, further validating the enhanced cycling stability and electrode kinetics of the OGCC-Li anode.[33]

Full cells were assembled by pairing OGCC-Li and Cu foil-Li anodes with a LFP cathode. Fig. 5a illustrates the long-term cycling performance of both LFP||OGCC-Li and LFP||Cu foil-Li cells. Remarkably, the LFP||OGCC-Li cell with a negative electrode capacity to positive electrode capacity (N/P) ratio of 13.7 achieves an initial capacity of 129 mA h g^{-1} and exhibits an impressive capacity retention of 92.6% over 300 cycles at a rate of 1 C. The remarkable cycling ability of the OGCC-Li electrode significantly outperforms that of the Cu foil-Li counterpart, which only retains 51% capacity. The rate performance was evaluated at varying current rates from 0.2 to 3 C. As depicted in Fig. 5b, at 0.2 C, the LFP||OGCC-Li cell delivers a maximum initial capacity of 150 mA h g^{-1}, surpassing the 143 mA h g^{-1} of the LFP||Cu foil-Li cell. The capacity disparity between the cells widens at higher C rates. Notably, at 3 C, the LFP||OGCC-Li cell maintains a reversible capacity exceeding 100 mA h g^{-1}, considerably higher than the 76 mA h g^{-1} observed in the LFP||Cu foil-Li cell. Impressively, when the current rate is reset to 0.2 C, the discharge capacity of the LFP||OGCC-Li cell is fully restored to 151 mA h g^{-1}. Additionally, the LFP||OGCC-Li cell exhibits smaller voltage polarization across different current rates (Fig. 5c and d), demonstrating superior electrochemical reversibility compared to the LFP||Cu foil-Li cell. Furthermore, the LFP||OGCC-Li cell is successfully used to power an indoor hygrothermograph, which operates stably for over two weeks (Fig. 5e), showcasing the practical application potential of the OGCC-Li anode.

4. Conclusions

In summary, we have engineered a conductivity/lithiophilicity dual-gradient host by layering an OPAN film onto a rGO-Cu_2O coated Cu foil. This structure forms a conductive gradient where the conductivity sequentially increases from the OPAN layer to the rGO-Cu_2O layer and then to the Cu foil. This gradient directs electrons to accumulate at the bottom of the host material. Additionally, the OPAN and rGO-Cu_2O layers create a lithiophilic gradient, lowering the Li nucleation barrier and promoting Li nucleation preferentially at the bottom. The synergistic effect of these gradients facilitates uniform Li deposition from bottom to top within OGCC and mitigates volume expansion during deposition. As a result, the OGCC host demonstrates exceptional electrochemical performance. Under conditions of 1 mA cm^{-2} for 1 mA h cm^{-2}, OGCC maintains an average CE of 98.4% over 500 cycles. Even at 3 mA cm^{-2} for 3 mA h cm^{-2}, it cycles stably for 110 cycles with a CE of 98.2%. The symmetric cell equipped with OGCC-Li also exhibits stable cycling for 1600 h at 1 mA cm^{-2} for 1 mA h cm^{-2} with a minimal hysteresis voltage of only 12 mV. Additionally, the LFP||OGCC-Li full cell retains 92.6% of its capacity after 300 cycles at a current rate of 1 C, with an average decay rate of only 0.025% per cycle. This innovative approach offers a promising strategy for developing LMAs with enhanced safety and cycling stability.

Data availability

The data supporting this article have been included as part of the ESI.†

Conflicts of interest

There are no conflicts to declare.

Acknowledgements

This work was supported by the doctoral research start-up project of Xi'an Polytechnic University (107020670), the National Natural Science Foundation of China (22279104 and 61935017), and the National Key Research and Development Program of China (2020YFA0709900).

References

1 Y. Jie, C. Tang, Y. Xu, Y. Guo, W. Li, Y. Chen, H. Jia, J. Zhang, M. Yang, R. Cao, Y. Lu, J. Cho and S. Jiao, *Angew. Chem., Int. Ed.*, 2024, **63**, e202307802.
2 J. Yang, M. Li, Z. Sun, X. Lian, Y. Wang, Y. Niu, C. Jiang, Y. Luo, Y. Liu, Z. Tian, Y. Long, K. Zhang, P. Yu, J. Zhang, Z. Wang, G. Wu, M. Gu and W. Chen, *Energy Environ. Sci.*, 2023, **16**, 3837–3846.
3 Y. Liu, Y. Li, Z. Du, C. He, J. Bi, S. Li, W. Guan, H. Du and W. Ai, *Adv. Sci.*, 2023, **10**, 2301288.
4 Q. Wang, T. Lu, Y. Liu, J. Dai, L. Guan, L. Hou, H. Du, H. Wei, X. Liu, X. Han, Z. Ye, D. Zhang, Y. Wei and H. Zhou, *Energy Storage Mater.*, 2023, **55**, 782–807.

5 Z. Du, W. Guan, C. He, Y. Liu and W. Ai, *Energy Storage Mater.*, 2024, **65**, 103191.
6 H. J. Liang, H. H. Liu, J. Z. Guo, X. X. Zhao, Z. Y. Gu, J. L. Yang, X. Y. Zhang, Z. M. Liu, W. L. Li and X. L. Wu, *Energy Storage Mater.*, 2024, **66**, 103230.
7 Y. Fang, Y. Zeng, Q. Jin, X. F. Lu, D. Luan, X. Zhang and X. W. Lou, *Angew. Chem., Int. Ed.*, 2021, **60**, 8515–8520.
8 Y. Zhang, M. Yao, T. Wang, H. Wu and Y. Zhang, *Angew. Chem., Int. Ed.*, 2024, **63**, e202403399.
9 Y. He, L. Song, Z. Li, X. Yao and Z. Peng, *Nano Energy*, 2023, **118**, 109027.
10 Y. Fang, S. L. Zhang, Z. Wu, D. Luan and X. W. Lou, *Sci. Adv.*, 2021, **7**, eabg3626.
11 W. Wu, D. Ning, J. Zhang, G. Liu, L. Zeng, H. Yao, M. Wang, L. Deng and L. Yao, *Energy Storage Mater.*, 2023, **63**, 102974.
12 J. W. Kang, J. H. Choi, J. K. Lee and Y. C. Kang, *J. Mater. Chem. A*, 2024, **12**, 7670–7679.
13 Y. Liu, J. Sun, X. Hu, Y. Li, H. Du, K. Wang, Z. Du, X. Gong, W. Ai and W. Huang, *Nano Energy*, 2022, **94**, 106883.
14 L. Ruan, X. Qin, K. Lin, Z. Yang, Q. Cai, T. Li, F. Wu, F. Kang and B. Li, *Nano Res.*, 2023, **16**, 4917–4925.
15 C. Sun, A. Lin, W. Li, J. Jin, Y. Sun, J. Yang and Z. Wen, *Adv. Energy Mater.*, 2020, **10**, 1902989.
16 W. Guan, X. Hu, Y. Liu, J. Sun, C. He, Z. Du, J. Bi, K. Wang and W. Ai, *Research*, 2022, **2022**, 9846537.
17 J. Sun, Y. Liu, L. Liu, S. He, Z. Du, K. Wang, L. Xie, H. Du and W. Ai, *Nano Lett.*, 2022, **22**, 3728–3736.
18 Y. Liu, W. Guan, S. Li, J. Bi, X. Hu, Z. Du, H. Du, W. Ai and W. Huang, *Adv. Energy Mater.*, 2023, **13**, 2302695.
19 W. Tang, J. Ma, X. Zhang, Y. Li, S. Meng, Y. Zhang, H. Dong, R. Liu, R. Gao and M. Feng, *Energy Storage Mater.*, 2024, **64**, 103084.
20 J. Bi, Z. Du, J. Sun, Y. Liu, K. Wang, H. Du, W. Ai and W. Huang, *Adv. Mater.*, 2023, **35**, 2210734.
21 J. Cao, G. Qian, X. Lu and X. Lu, *Small*, 2023, **19**, 2205653.
22 H. Qian, X. Li, Q. Chen, W. Liu, Z. Zhao, Z. Ma, Y. Cao, J. Wang, W. Li, K. Xu, K. Zhang, W. Yan, J. Zhang and X. Li, *Adv. Funct. Mater.*, 2024, **34**, 2310143.
23 C. Shi, J. Huang, Z. Cen, T. Yi, S. Liu and R. Fu, *Carbon*, 2024, **217**, 118616.
24 P. Techaniyom, P. Tanurat and S. Sirivisoot, *Appl. Surf. Sci.*, 2020, **526**, 146646.
25 S. Kim, J. A. Lee, T. K. Lee, K. Baek, J. Kim, B. Kim, J. H. Byun, H. W. Lee, S. J. Kang, J. A. Choi, S. Y. Lee, M. H. Choi, J. H. Lee and N. S. Choi, *Energy Environ. Sci.*, 2023, **16**, 5108–5122.
26 Y. Bao, Y. S. Tay, T. T. Lim, R. Wang, R. D. Webster and X. Hu, *Chem. Eng. J.*, 2019, **373**, 425–436.
27 N. Li, K. Zhang, K. Xie, W. Wei, Y. Gao, M. Bai, Y. Gao, Q. Hou, C. Shen, Z. Xia and B. Wei, *Adv. Mater.*, 2020, **32**, 1907079.
28 J. Bi, Y. Liu, Z. Du, K. Wang, W. Guan, H. Wu, W. Ai and W. Huang, *Adv. Mater.*, 2024, **36**, 2309339.
29 X. Li, Y. Su, Y. Qin, F. Huang, S. Mei, Y. He, C. Peng, L. Ding, Y. Zhang, Y. Peng and Z. Deng, *Adv. Mater.*, 2023, **35**, 2303489.
30 Y. Liu, C. He, J. Bi, S. Li, H. Du, Z. Du, W. Guan and W. Ai, *Small*, 2024, **20**, 2305964.
31 Y. Liu, Y. Li, J. Sun, Z. Du, X. Hu, J. Bi, C. Liu, W. Ai and Q. Yan, *Nano Res. Energy*, 2023, **2**, e9120048.
32 Y. N. Liu, J. L. Yang, Z. Y. Gu, X. Y. Zhang, Y. Liu, M. Y. Su, X. L. Zhang, I. V. Zatovsky, K. Li, J. M. Cao and X. L. Wu, *Angew. Chem., Int. Ed.*, 2024, **63**, e202316925.
33 T. Naren, G. Kuang, R. Jiang, P. Qing, H. Yang, J. Lin, Y. Chen, W. Wei, X. Ji and L. Chen, *Angew. Chem., Int. Ed.*, 2023, **62**, e202305287.